Electronic Supplementary Material (ESI) for Energy & Environmental Science.

Supplementary Information for "Optical Properties and Limiting Photocurrent of Thin-Film Perovskite Solar Cells"

James M. Ball,‡[1] Samuel D. Stranks,¶[1] Maximilian T. Hörantner,[1] Sven Hüttner,§[2‡] Wei Zhang,[1] Edward J. W. Crossland,[3] Ivan Ramirez,[1] Moritz Riede,[1] Michael B. Johnston,[1] Ullrich Steiner,[2] and Henry J. Snaith[1]*

[1]University of Oxford, Clarendon Laboratory, Parks Road, Oxford, OX1 3PU, United Kingdom
[2]University of Cambridge, Cavendish Laboratory, JJ Thomson Avenue, Cambridge, CB3 0HE, United Kingdom
[3]Oxford Photovoltaics, Begbroke Science Park, Begbroke Hill, Woodstock Road, Begbroke, Oxfordshire, OX5 1PF, United Kingdom

*Author to whom correspondence should be addressed, e-mail: henry.snaith@physics.ox.ac.uk
‡ Current address: Istituto Italiano di Tecnologia, Center for Nanoscience and Technology, Via Pascoli 70/3, 20133 Milano, Italy
¶ Current address: Massachusetts Institute of Technology, 77 Massachusetts Avenue, Cambridge, MA, 02141, United States.
§ Current address: Macromolecular Chemistry I, University of Bayreuth, Universitätstr. 30, 95447 Bayreuth, Germany

S1. SPECTROSCOPIC ELLIPSOMETRY

The glass substrate coated with a transparent conductive oxide (FTO glass) is assumed to be multilayer stack,[1,2] as shown in Figure S1a. Literature values were taken for the optical constants and dielectric functions.[2] The derived thicknesses of the FTO, SiO_2, and SnO_2 were 339.898±0.139 nm, 23.246±0.065 nm, and 27.723±0.0569 nm, respectively. The best fit to the ellipsometry data for the FTO glass stack included a layer accounting for the surface roughness as an effective medium using the Bruggeman approximation[3,4] with a thickness of 29.130±0.0736 nm and a volume ratio of FTO:air of ~0.65:0.35. To verify that making this approximation in the transfer-matrix model is valid we compared the predicted and measured transmission spectra based on these data, as shown in Figure S1b, and obtain good agreement. The optical constants for the discrete layers in the stack are shown in Figure S2.

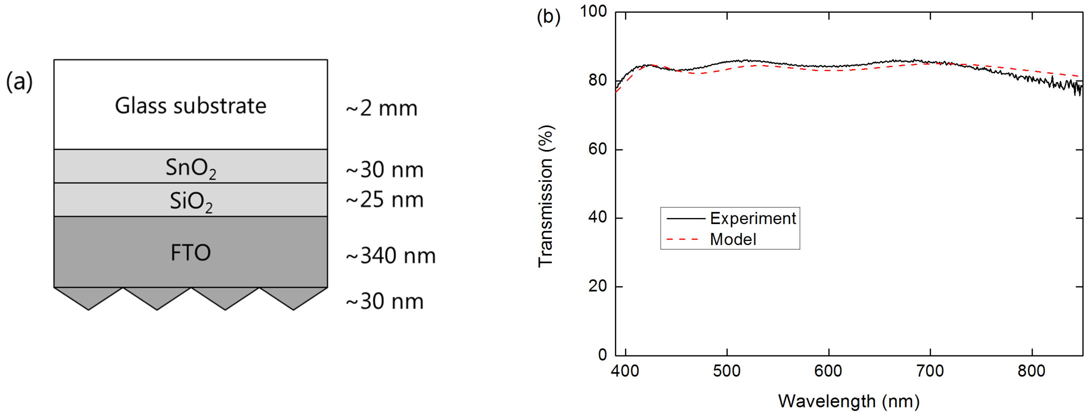

Figure S1. (a) Multilayer stack used in the ellipsometry model for extracting the optical constants for the FTO-coated soda-lime glass substrate, and (b) comparison of experimental and transfer-matrix modelled transmission spectrum.

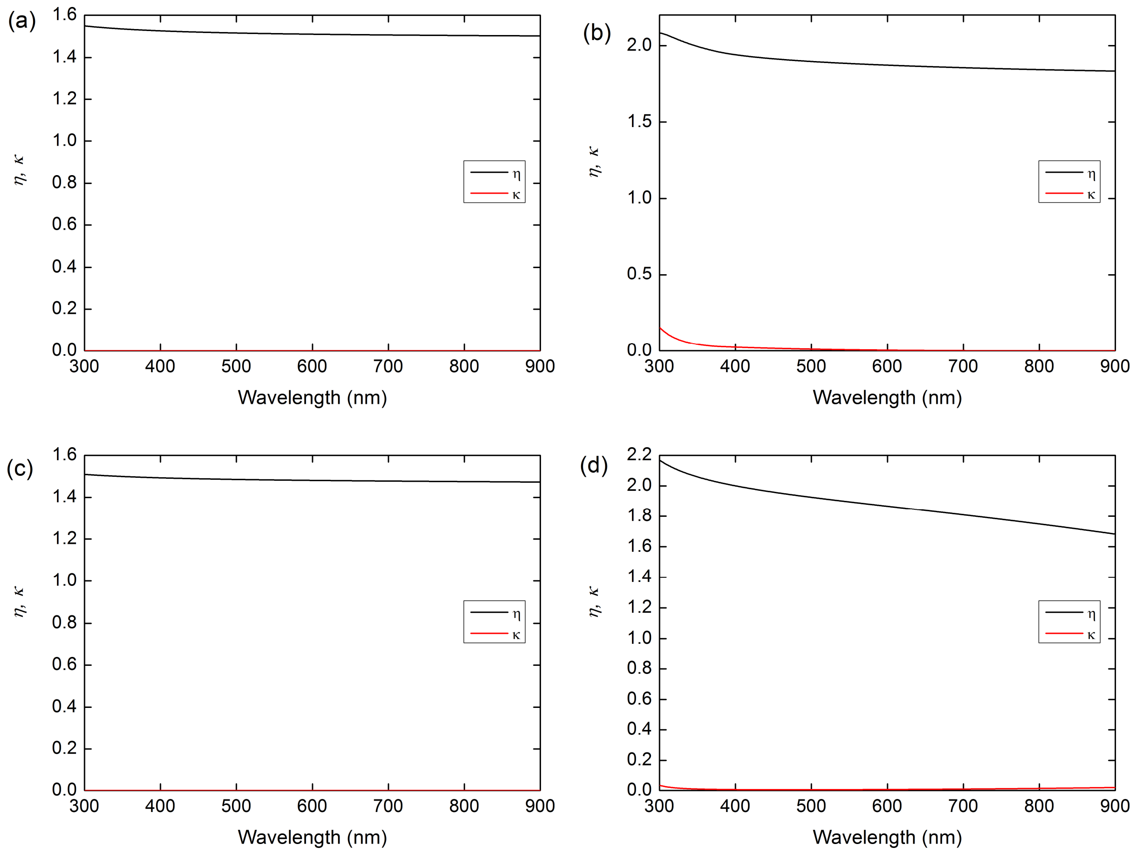

Figure S2. Complex refractive index spectra for the layers of a Pilkington TEC 15 glass substrate coated with transparent conductive oxide. (a) Glass, (b) SnO_2, (c) SiO_2, and (d) FTO.

The complex refractive indices for the TiO_2 compact layer, and Spiro-OMeTAD derived from the analysis of spectroscopic ellipsometry measurements are detailed in Figure S3. The TiO_2 film was first fit with a Cauchy layer model in the range between 500-900 nm, where the material shows no significant absorption. The thickness was fitted as 40.995±0.033 nm (with a MSE of 1.86). This thickness was kept constant and a respective gliding average of the point-to-point fit was applied to derive the optical constants.

Ellipsometry measurements of a pristine Spiro-OMeTAD film was first fit with a Cauchy layer model in the range between 500-900 nm, where the material shows no significant absorption. The thickness was fitted as 263.68 nm (with a MSE of 2.003). This thickness was kept constant and a respective gliding average of the point-to-point fit was applied to derive the optical constants.

In devices, Spiro-OMeTAD is doped giving rise to an absorption feature in the visible. Due to difficulties in making uniform thin-films doped with Li-salt on SiO_2 wafers, the optical constants are derived based on a film doped at 5 mol% with Spiro(tfsi)$_2$.[5,6] The doped Spiro-OMeTAD film was first fit with a Cauchy layer model in the range between 800-900 nm, where the material shows no significant absorption. The thickness was fitted as 223.540 nm (with a MSE of 2.904). This thickness was kept constant and a respective gliding average of the point-to-point fit was applied to derive the optical constants. For the transfer matrix model, the Spiro-OMeTAD layer is implemented as an Bruggeman effective medium[3,4] of the pristine film and a film doped with Spiro(tfsi)$_2$. Based on the relative conductivities of the layers in comparison to the Li-salt doped film, the volume fraction of the 5 mol% doped component is ~10% in the effective medium.

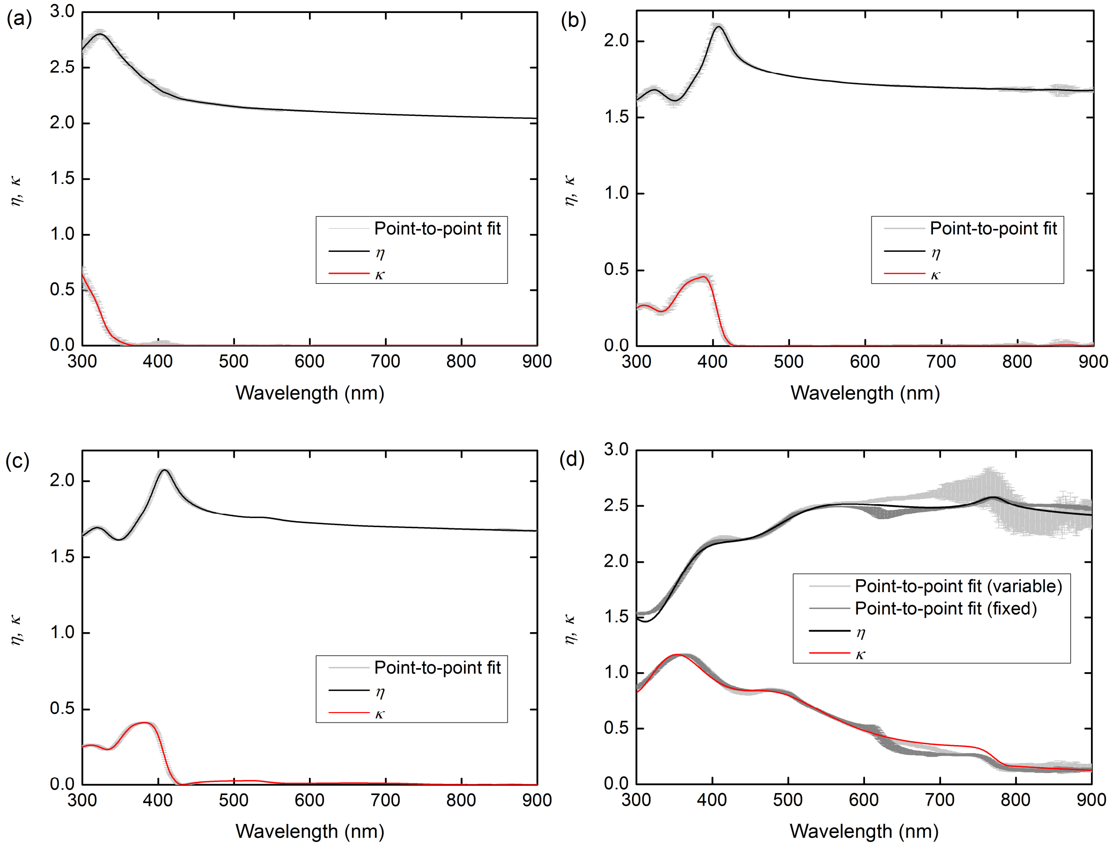

Figure S3. Experimentally derived complex refractive index spectra for (a) TiO2, (b) pristine Spiro-OMeTAD, (c) Spiro-OMeTAD doped at 5 mol% with Spiro(tfsi)$_2$, and (d) $CH_3NH_3PbI_3$ (showing two possible point-to-point fits: either with variable thicknesses, or at fixed thickness as indicated).

The initial thickness of the perovskite film for ellipsometry was estimated in a wavelength range between 780 – 900 nm, where only a little absorption took place. A thickness of 141.24 nm was measured, which corresponds to the value of the thickness measured using profilometry. A point-to-point fit was performed with both a fixed thickness, and variable thickness as shown in Figure S3d. To derive data for the transfer-matrix model, we applied a simplified arbitrary oscillator model which corresponds to the main transitions in the perovskite material with sufficient accuracy (one Tauc-Lorentz oscillator with a band gap of 1.56 eV and 3 Lorentz oscillators, parameters given in Table S1). The energy offset was 2.47 eV. More complicated oscillator models as demonstrated in other elaborate spectroscopic ellipsometry studies on III-V semiconductors are beyond the scope of this study and require extremely high quality films as well as detailed knowledge on the theoretical expression of the energy-band parameters.[7,8]

TABLE S1. Summary of parameters used in the oscillator model describing the pseudodielectric function of $CH_3NH_3PbI_3$.

Oscillator	Amplitude	Energy (eV)	Broadening
Tauc-Lorentz	45.82	1.6008	0.11507
Lorentz 1	2.1796	2.5026	0.95394
Lorentz 2	2.4127	2.5026	0.95394
Lorentz 3	3.6701	3.4353	1.2071

For the methylammonium lead iodide layer, with the extracted complex refractive index it is also possible to derive the absorption coefficient from the extinction coefficient as well as the complex dielectric constant at optical frequencies. The absorption coefficient in comparison to other literature data[9–11] is shown in Figure S4.

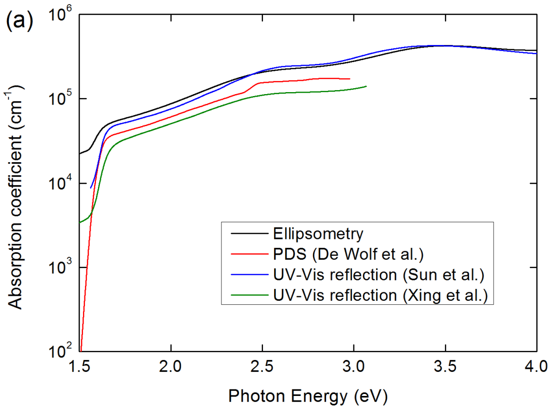

Figure S4. The absorption coefficient of methylammonium lead iodide measured in the present work in comparison to literature data.[9–11]

S2. TRANSFER-MATRIX MODELLING

The model is written in Python v2.7 and makes extensive use of the open-source module "tmm", developed by Steve Byrnes,[12] which is implemented as a wrapper for solar cells. The solar cell wrapper was developed to conveniently import refractive index data from a .csv file and use the returned values from the tmm-module for the calculation of reflectivity, absorptivity in all layers, transmissivity, electric-field, generation rate and J_{sc}. Updates and future versions of the code can be downloaded freely from https://github.com/matoho/tmm_solarcell.

The tmm-module employs the transfer matrix formalism for general optical calculations of multi-layer structures and is thoroughly documented elsewhere.[13] It offers convenient methods to calculate the Fresnel coefficients at every interface for a whole stack of coherently and incoherently treated layers. The complex refractive indices as a function of wavelength, thicknesses, and whether a layer should be treated coherently of incoherently (thick layers compared to the incident wavelength should be treated as incoherent where all interference effects are neglected) for every layer are passed as the input parameters. Then the method returns the Fresnel coefficients, the fractions of reflected and transmitted intensity, the forward and backward travelling electric-field at every interface, absorption in every layer, electric-field as a function of stack depth, charge generation rate as a function of stack depth, total reflection, total transmission and total absorption at every specified wavelength.

The calculations are carried out separately for s- and p-polarization and finally averaged assuming 50% s- and 50% p-polarized for realistic sun-light conditions (although any combination of polarisation states for alternative light sources can easily be accommodated). The tmm-solver processes the transfer matrices at every interface and distinguishes between incoherent and coherent layers, which the user defines previously. The Fresnel coefficients at the first and last interface are used to evaluate the fraction of light that gets reflected from and transmitted through the whole stack. Furthermore, the Poynting vectors are resolved at every interface. The difference of its normal components between the two interfaces of a layer leads to the absorbed power. Summing over all layers leads to the total absorption that equals $A_{tot}=1-R_{tot}-T_{tot}$, to numerical accuracy, at every wavelength. Additionally, the forward and backward travelling E-fields at every interface are returned by the tmm solver and are then resolved at every position within the layers in all three dimensions according to Young et al.[14]

Numerically integrating the absolute amplitude of the E-field intensity over the whole solar spectrum leads to the charge generation at every position that can be simply converted to the J_{sc}, when assuming that all generated charges contribute to the current (IQE = 100%). J_{sc} losses are separated in losses from reflectance, and losses from photons absorbed in other layers. They can be computed via the spectral power loss for the spectra from reflection and parasitic absorption. Notably, all values are separately calculated for s- and p-polarization allowing alternative light sources to be simulated. Alternatively, the code allows calculation of J_{sc} as a function of angle and thickness from integration of a derived IQE (from one measurement assuming invariance with angle and thickness), LHE and incident power density.[15] Example output from the model, in addition to calculations of total reflection, absorption and transmission, includes the distribution of the electric field and the charge generation profile as shown in Figure S5.

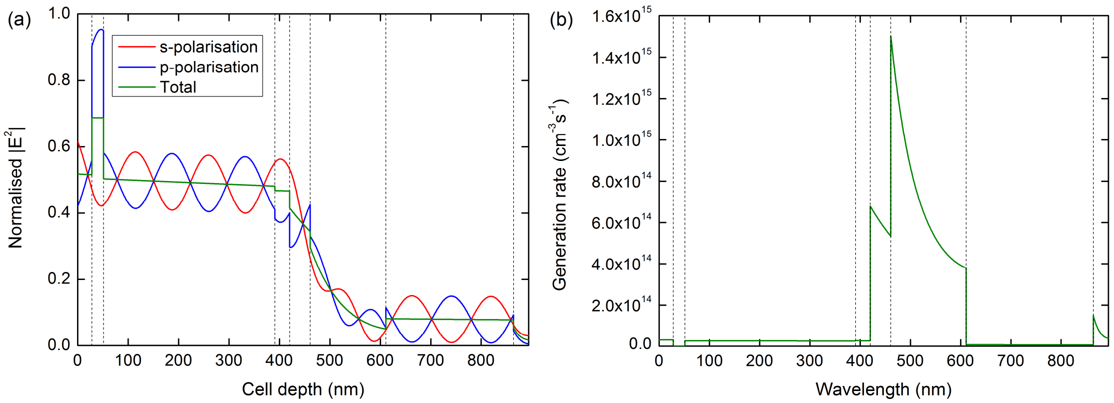

Figure S5. Example output from the transfer-matrix model. (a) The total, s-polarised, and p-polarised optical electric field distributions for incident light at 550nm. (b) The distribution of the total generation rate within the optical stack derived from the power dissipation from the electric field.

S3. SOLAR CELL CHARACTERISATION

S3.1 Solar simulator calibration

For an accurate analysis of the current-voltage characteristics of a solar cell, the spectrum of the simulation lamp must be known. The spectral shape was measured using a MAYA Ocean Optics spectrophotometer which was calibrated using a certified tungsten lamp (Newport) to correct for spectral intensity attenuation of the optical system, and a mercury lamp to correct the CCD detector for wavelength offsets. This yields a relative spectrum. The absolute power density is calculated by deriving a correction factor from a measurement of the current generated in an NREL certified silicon photodiode with a KG5 filter illuminated by the solar simulator. The measured spectrum of the solar simulator and standard AM 1.5 G solar spectrum are given in Figure S6. In the spectral region of the measured EQE, the mismatch factor[15–17] is 1.057. Given the intensity of the lamp during the measurement, this means the solar cell was measured under and effective irradiance of 104.7 mW/cm^2, or 1.047 suns.

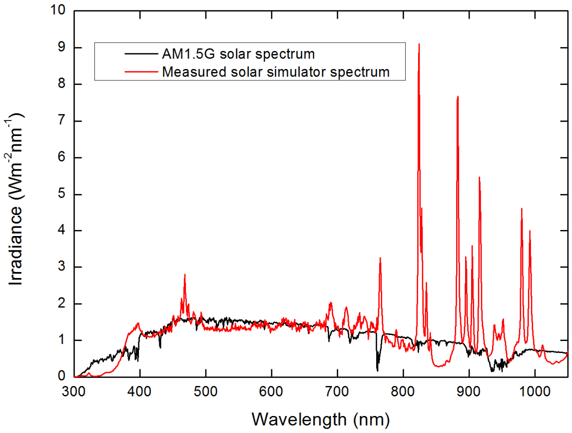

Figure S6. Comparison of the standard AM1.5G solar spectrum and our measured solar simulator spectrum.

S3.2 Comparison to finite-difference time domain simulations

An additional comparison of the optical properties of the device using our method was made based on finite-difference time domain (FDTD) numerical simulations using the Lumerical software package.[18]

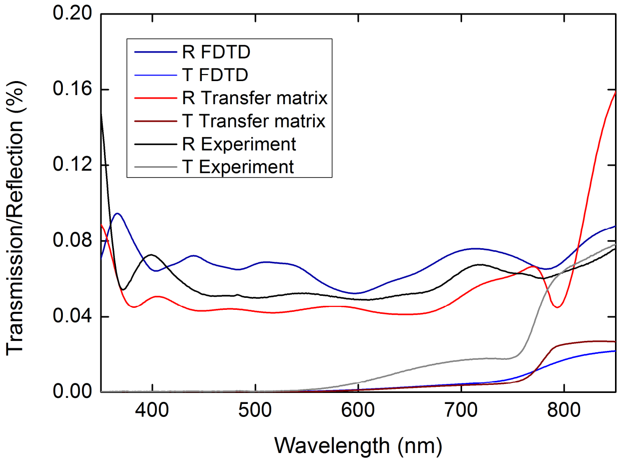

Figure S7. Comparison between FDTD simulation, transfer matrix simulation and experimental measurements for the reflection and transmission spectra for the perovskite device.

The treatment of mixed incoherent and coherent layers is more challenging with reasonable computation times using this approach so we invoke the approximation that the glass layer is only 20 µm thick, and evaluate the simulation centred at each wavelength with a Lorentzian weighting function. The comparison between FDTD, transfer matrix and experimental data are shown in Figure

S7. Both simulation methods reproduce the prominent features of the experimental spectra with a similar level of deviation.

S3.3 Current-voltage and external quantum efficiency measurements

The current density-voltage characteristic of the device used for verification of the transfer matrix model are given in Figure S8.

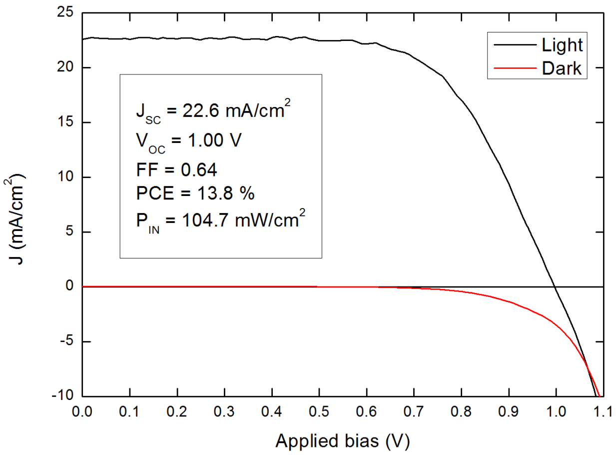

Figure S8. J-V characteristic of the device used for validation of the transfer-matrix model, scanning from forward bias to short-circuit.

The spectral shape of the external quantum efficiency was measured using Fourier-transform Photocurrent Spectroscopy (FTPS). The raw measurement was corrected for the shape of the power spectrum of the incident light source using a Si reference photodiode. The relative spectrum was then scaled to give an equivalent integrated short-circuit current to the cell under the solar simulator spectrum given in Figure S6. Excluding the possible photocurrent generated from the solar simulator below 340 nm, the lower limit for the measurement, leads to an error of negligible error of < 0.2% in the correction factor.

S3.4 Comparison to integrating sphere measurements

The origin of uncertainty in the standard integrating sphere approach, where the absorption in each layer is measured in isolation, arises from the approximation that internal reflections, when the layers are brought together, in the device can be neglected. In general, the propagation of light through the stack depends on the interfaces between the layers through the Fresnel reflection and transmission coefficients, and the resulting interference condition. Therefore, the proportion of light reaching and absorbed by each layer of the stack depends on the stack in its entirety, not on the layers in isolation. This means the uncertainty in the results when making the integrating sphere approximations cannot be generalised and is specific to the stack, i.e. it cannot be known whether the approximation is valid without additional information.

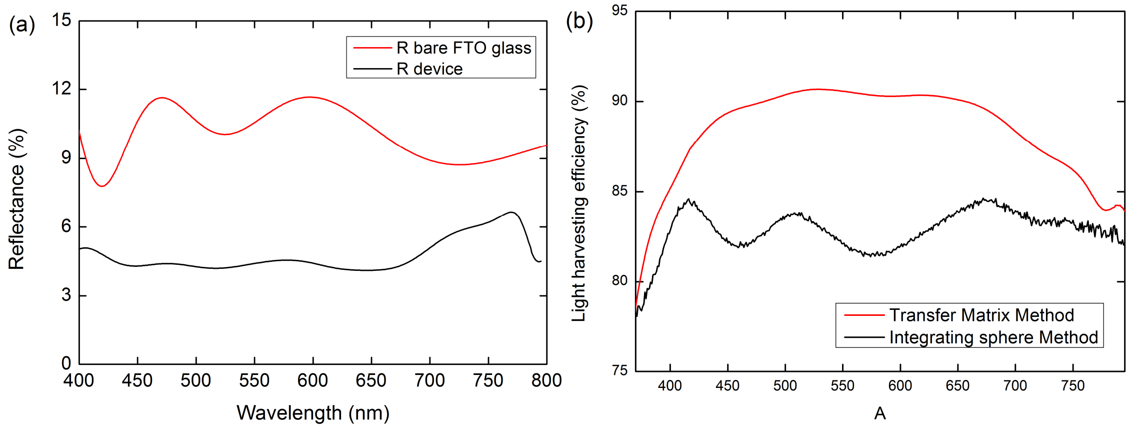

Figure S9. (a) Comparison between modelled reflectance spectra of bare FTO glass and the complete device. (b) Comparison between the light-harvesting efficiency of the active layer calculated using the transfer-matrix method and the integrating sphere method.

As an example, we highlight how this is manifest for our perovskite-based solar cell. For the integrating sphere approach we assume that the majority of parasitic absorption occurs in the FTO glass but that reflections at its interfaces can be neglected.[19] Figure S9a shows the modelled reflectance spectra comparison between the bare FTO glass (as used for the integrating sphere approach to isolate its contribution) and in the complete device. The bare FTO glass gives more reflectance than the device because the index matching at the outgoing FTO/air interface produces a larger reflection coefficient than the interface between FTO and the subsequent layers in the device stack. Using the bare FTO glass will therefore produce a different value for its absorption than when subsequent layers are coated on it. Figure S9b shows the comparison of the active layer absorption spectra based on the integrating sphere approach where the light-harvesting efficiency (LHE) is estimated using the bare FTO absorption and the device reflectance,[19] and the transfer matrix method.

This suggests that using the integrating sphere for this particular device could lead to a systematic underestimation of the LHE of up ~10% over a significant proportion of the visible spectrum. Put another way, we would assume an EQE measurement of over 85% was unphysical if using the integrating sphere measurement, whereas it is clearly possible to achieve EQE over 90% following the complete optical modelling.

S3.5 Thickness dependence and uncertainty

As an example optimisation that can be performed using the transfer matrix model, we investigated the dependence of the short-circuit current density on active layer thickness, assuming that the IQE shown in Figure 4a is valid for all thicknesses. This simulation uses the unpolarised AM 1.5 spectrum. A device relevant thickness range is shown in Figure S10a. The graph suggests that near maximum light absorption can be achieved for thicknesses of >300 nm and that local minima due to unfavourable interference conditions are weak. The influence of enhanced visible absorption due to oxidised Spiro-OMeTAD is compared to the effective medium used throughout the manuscript is also shown in Figure S10a. The additional parasitic absorption is minimal and only has an influence for very thin perovskite layers.

We also explored the thickness dependence of the contact layers, TiO_2 and Spiro-OMeTAD, for thin and thick perovskite layers, as we show in Figure S10b and c. For optically thick perovskite films, where almost all of the light that reaches the active layer is absorbed within it, device relevant thickness variations lead to weak interference maxima and minima in the predicted J_{sc}. Reducing the perovskite thickness, allowing more light to propagate through it, leads to interference effects become stronger and therefore a stronger dependence of the predicted J_{sc} on contact layer thickness.

Formally, the propagation of thickness errors is seldom included in the transfer matrix method (we could find no examples in the literature) principally because the complexity of the calculation does not easily facilitate conventional error analysis within an acceptable timescale on a desktop computer. However, in the present case, by iterating the simulation over a reasonable thickness range as shown in Figures 4b, S10b and S10c we can determine that in the limit of an optically thick device relevant active layer, the thickness uncertainty is expected to form a minor contribution.

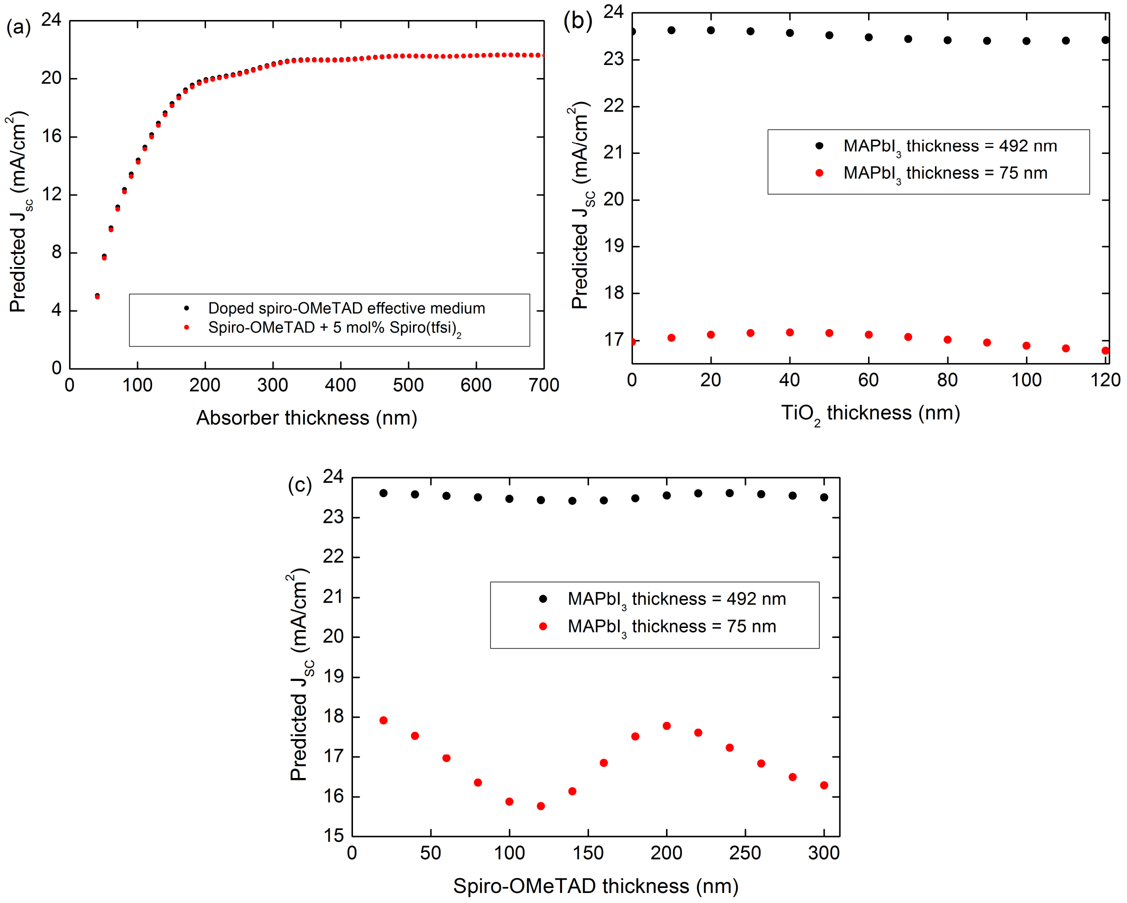

Figure S10. Simulated dependence of J_{sc} on (a) active-layer thickness with a comparison between two levels of Spiro-OMeTAD oxidation, (b) TiO_2 thickness between the FTO and perovskite interfacial effective media, and (c) Spiro-OMeTAD thickness.

S3.6 Angular dependence

To verify that the optical model accurately reflects the real device performance for incident angles away for normal incidence, we measured the device short-circuit current density as a function of incident angle using a laser light source (TEM_{00} mode so s-polarised light can be neglected, linearly polarised, 532 nm, CW). The experimental setup is shown in Figure S11a and the comparison of the data between the model and experiment is shown in Figure S11b, providing good agreement.

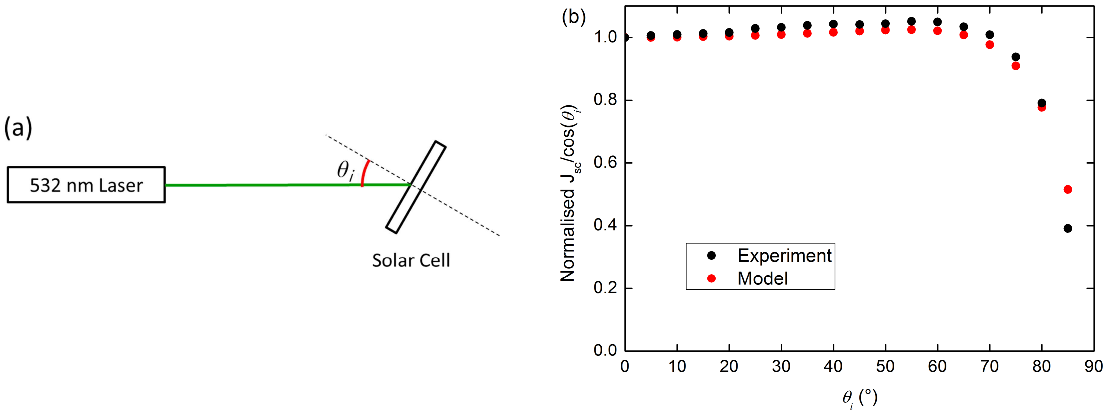

Figure S11. (a) Experimental setup for angular dependent measurements. (b) Comparison of the normalised angular dependence of J_{sc} between the experiment and the transfer-matrix model.

REFERENCES

1. S. Kohli, V. Manivannan, J. N. Hilfiker, P. R. McCurdy, R. A. Enzenroth, K. L. Barth, W. P. Smith, R. Luebs, and W. S. Sampath, *J. Sol. Energy Eng. Asme*, 2009, **131**, 7.

2. Jie Chen, in *Spectroscopic ellipsometry studies of II-VI semiconductor materials and solar cells*, 2010, p. Paper 807.

3. D. A. G. Bruggeman, *Ann. Phys.*, 1935, **416**, 969–664.

4. R. Landauer, *J. Appl. Phys.*, 1952, **23**, 779–784.

5. A. Abate, T. Leijtens, S. Pathak, J. Teuscher, R. Avolio, M. E. Errico, J. Kirkpatrik, J. M. Ball, P. Docampo, I. McPherson, and H. J. Snaith, *Phys. Chem. Chem. Phys.*, 2013, **15**, 2572–9.

6. W. H. Nguyen, C. D. Bailie, E. L. Unger, and M. D. McGehee, *J. Am. Chem. Soc.*, 2014, **136**, 10996–11001.

7. S. Ozaki and S. Adachi, *J. Appl. Phys.*, 1995, **78**, 3380–3386.

8. G. N. Maracas, C. H. Kuo, S. Anand, and R. Droopad, *J. Appl. Phys.*, 1995, **77**, 1701–1704.

9. S. De Wolf, J. Holovsky, S. J. Moon, P. Löper, B. Niesen, M. Ledinsky, F. J. Haug, J. H. Yum, and C. Ballif, *J. Phys. Chem. Lett.*, 2014, **5**, 1035–1039.

10. S. Sun, T. Salim, N. Mathews, M. Duchamp, C. Boothroyd, G. Xing, T. C. Sum, and Y. M. Lam, *Energy Environ. Sci.*, 2014, **7**, DOI: 10.1039/c3ee43161d.

11. G. Xing, N. Mathews, S. Sun, S. S. Lim, Y. M. Lam, M. Grätzel, S. Mhaisalkar, and T. C. Sum, *Science*, 2013, **342**, 344–7.

12. S. Byrnes, *http://sjbyrnes.com/?page_id=12*, Accessed 22nd September 2014.

13. S. Byrnes, *http://sjbyrnes.com/fresnel_manual.pdf*, Accessed 22nd September 2014.

14. M. Young, C. J. Traverse, R. Pandey, M. C. Barr, and R. R. Lunt, *Appl. Phys. Lett.*, 2013, **103**.

15. H. J. Snaith, *Energy Environ. Sci.*, 2012, 5, 6513.

16. National ASTM standard E948, .

17. I. standard 60904-1, .

18. Lumerical, *https://www.lumerical.com/tcad-products/fdtd/*, Accessed 14th November 2014.

19. J. M. Ball, M. M. Lee, A. Hey, and H. J. Snaith, *Energy Environ. Sci.*, 2013, **6**, 1739–1743.